# A Time Domain Approach for Shock Noise Prediction with Decomposition Analyses of Large-Scale Coherent Turbulent Structures in Jets

Weiqi Shen, Trushant K. Patel, and Steven A. E. Miller

*Department of Mechanical and Aerospace Engineering, University of Florida, Gainesville, FL, 32611, USA*

**Abstract**

Broadband shock-associated noise (BBSAN) is one dominant component from off-design supersonic jets. A time-domain BBSAN model is proposed and evaluated, which is based on the vector Green's function solution of the decomposed Navier-Stokes equations. The source term is the scalar product of the anisotropic velocities with the mean pressure gradient. The approach uses large-eddy simulation (LES) databases. Proper orthogonal decomposition (POD) is applied to the scalar source field to extract the large-scale coherent structures associated with BBSAN. The key features of the BBSAN spectra are preserved when only a small fraction of POD modes are used to reconstruct the source field. The leading POD modes of the source term show strong amplification in the observer direction. Noise source contour plots calculated with these POD modes reveal that most noise sources are distributed at the shock-turbulence interactions. Predictions are validated with the Ffowcs Williams and Hawkings method and experimental data.

*Keywords:* Large Eddy Simulation, Broadband Shock-Associated Noise, Proper Orthogonal Decomposition, Time Domain

## 1. Introduction

Noise generated by the exhaust from high-performance military aircraft is a major health concern for the military personnel who work on the flight decks of aircraft carriers. According to Doychak [1], the noise level on the flight deck can be as loud as 150 dB, especially in the downstream direction relative to the nozzle exit. Constant exposure to such an extreme environment can

lead to service-related disabilities such as tinnitus and hearing loss even with hearing protection, which costs the U.S. government billions of dollars every year in health costs.

Jet noise is mainly generated by turbulent mixing of the jet exhaust with the ambient air. Turbulent flow was recognized as an assemblage of chaotic motions in early studies [2], until the existence of organized flow features were first found by Townsend [3]. A comprehensive review of coherent structures was carried out by Hussain [4]. Later, large-scale coherent structures were identified in different types of turbulent flows [5, 6, 7] including shear layers and axisymmetric jets. The scales of these coherent structures greatly exceed the integral scales of the turbulence, making them a more efficient source of noise than the random fine-scale turbulent mixing. The large-scale turbulent structures are the dominant source of noise in high speed subsonic and supersonic jets [8].

In order to model the coherent structures in jet flows and eventually predict noise produced by them, various theories based on either empirical or analytical approaches were proposed. One of the most popular approaches was proposed by Tam and Chen [9], which models the large-scale coherent structures as a superposition of instability waves initiated by random excitation at the nozzle lip. Acoustic radiation by instability waves in different types of flow were also predicted by Tam et al. [10, 11, 12]. Later, a wave packet theory [13] was proposed to model the coherent structures using experimental measurement of the acoustic field or near-field velocity.

Military engines usually operate at off-design conditions during take-off, which create a quasi-periodic shock-cell structure within the jet plume. These quasi-periodic shock-cell structures interact with large-scale turbulent structures in the jet shear layer, creating strong noise radiation in the sideline and upstream directions, known as the broadband shock-associated noise (BBSAN). Previous prediction methods of BBSAN, which we review briefly, focus on creating models in the frequency domain. Here, we propose a model for BBSAN in the time-domain that depends on large-scale coherent turbulent structures and the shock-cell structure. We focus on the prediction of BBSAN by extracting the large-scale coherent structures from jet simulation databases.

### *1.1. Previous Methods*

The pioneering work on BBSAN was carried out by Harper-Bourne and Fisher [14], who modeled BBSAN as discrete shock-vortex interactions. The

noise was modeled for convergent nozzles using an array of point sources distributed along the shock locations at the lip-line of the jet. These point sources are correlated, creating strong noise radiation through constructive interference at observers in the far-field. Tam and Tanna [15] proposed that BBSAN is generated by the weak interaction between downstream propagating large-scale turbulent structures and the shock-cell structure of the jet. A noise intensity scaling formula and a peak frequency formula were derived using this framework. Tam [16] also integrated his stochastic model for instability waves with the shock-cell structures to predict the BBSAN spectra. In this model, the jet flow is viewed as a superposition of the waveguide modes with different wavelengths and the instability waves. Because of this superposition, the instability waves are scattered into different upstream directions. The upstream propagating waves that have supersonic phase speed generate noise through Mach wave radiation. Each waveguide mode has a different wavelength that generates a distinct noise spectrum with a spectral peak frequency. Therefore, the total shock noise spectrum is made up of the superposition of these spectra. This method successfully predicts the multiple broadband peaks in the noise spectrum and shows good agreement between the calculated and the measured spectra. Morris and Miller [17] developed an acoustic analogy to predict BBSAN based on linearized Euler equations using the solutions of Reynolds-averaged Navier-Stokes (RANS) equations. In their model, the use of RANS solutions enables the prediction of the BBSAN at a wide range of operating conditions as only nozzle geometry and operating conditions are required for the prediction. Alternatively, a wave-packet model was proposed by Suzuki [18] to predict BBSAN from a large eddy simulation (LES) database.

In the past few decades, with the development of numerical algorithms and high-performance computing, numerical approaches have become popular for jet noise prediction. Direct Numerical Simulation (DNS), that directly integrates the Navier-Stokes equations in time, requires the computational mesh to be fine enough to resolve the finest scale in the flow-field (Kolmogorov scale). Wilcox [19] suggested that the number of elements for DNS should scale with $\mathrm{Re}^{9/4}$, where Re is the Reynolds number of the flow. This scaling makes DNS prohibitively expensive for high Reynolds number flow. On the other hand, LES only resolves the most energetic scales in the turbulent flow, while modeling the smaller and less energetic scales using sub-grid scale models. The required number of elements estimated by Choi and Moin [20], is only of the order of $\mathrm{Re}^{13/7}$ for wall resolved LES and Re for wall modeled

LES, making it an affordable choice for jet simulations, while still being able to accurately resolve enough flow features. Therefore, LES coupled with a Ffowcs Williams and Hawkings (FWH) [21] acoustic solver to compute the far-field noise has become a popular method for the jet noise predictions.

Early LES of jet flows were carried out using finite difference methods (Boersma and Lele [22]). In these works, nozzle geometries were not included in the computational domain due to the difficulty of dealing with complex geometries using a structured mesh. Shur et al. [23] used a structured multiblock solver to predict the noise from jets of airliner engines, where the RANS solution inside of the nozzle was coupled with the LES freestream domain. Unstructured solvers [24, 25, 26] using the finite volume method simplify the modeling of the nozzle geometries and improve the accuracy of the simulations. Advanced techniques such as wall modelling, adaptive mesh refinement, and synthetic turbulence [27, 28, 29] were used at the nozzle inner wall boundary layer to obtain satisfactory far-field noise predictions. Recently, high-order discontinuous methods have been applied to jet simulations. Codes that use these methods such as the Jet Engine Noise Reduction (JENRE) code [30] and Glenn Flux Reconstruction (GFR) code [31] have shown great potential of generating accurate simulation results with less computational cost.

### *1.2. Present Approach*

Miller [32] proposed an acoustic solution to turbulent fields based on a decomposition of the equations of motion, which was first applied to a homogeneous isotropic turbulent field. The Navier-Stokes equations are decomposed into a time-averaged base flow, aerodynamic turbulent fluctuations, and acoustic fluctuations. The aerodynamic turbulent fluctuations are further decomposed into fluctuations from large-scale and fine-scale turbulent structures. The time-varying acoustic variables are calculated using the vector Green's function and the two-point cross-correlation of the right-hand side. These sources can be evaluated either using turbulence theories or from numerical simulations. The sources account for different components of noise.

We follow the methodology of Miller [32] and Patel and Miller [33] to predict the time-varying acoustic pressure from BBSAN, and validate the approach through comparison with far-field measured and FWH derived statistics. We apply POD to decompose the LES source field into spatial-temporal modes. The modes corresponding to the most significant sources of BBSAN

are identified and isolated. A time-domain approach is used to calculate the BBSAN from the reconstructed source field using the POD modes. The reconstructed BBSAN spectra and the total spectra predicted with the FWH method are compared with the experimental measurements. Finally, the source intensity distributions are presented to identify the major source locations.

## 2. Methodology

### *2.1. Numerical Methods*

The simulation results in the present paper are produced by the High Fidelity Large-Eddy Simulation (HiFiLES) solver originally developed by the Stanford Computational Aerodynamics lab [34]. The solver is based on the high-order flux reconstruction scheme, which was first proposed by Huynh [35] as a unifying approach to achieve high-order accuracy on unstructured grids. It was later extended to different types of elements [36, 37] and viscous problems [38, 39] to account for a wide range of practical problems. In the previous work, the HiFiLES solver has been modified to include new features such as shock capturing methods and numerical probes for supersonic jet acoustic simulations (see Shen and Miller [40]). In this section, we will briefly review the numerical methods used in the solver.

The HiFiLES LES code solves the Favre-filtered Navier-Stokes equations

$$\frac{\partial \mathbf{q}}{\partial t} + \nabla \cdot \mathbf{F} = 0, \tag{1}$$

where the solution variables $\mathbf{q}$ and the flux $\mathbf{F}$ are given by

$$\mathbf{q} = \begin{bmatrix} \bar{\rho} \\ \bar{\rho}\tilde{u}_i \\ \bar{\rho}\tilde{E} \end{bmatrix}, \qquad \mathbf{F} = \begin{bmatrix} \bar{\rho}\tilde{u}_j \\ \bar{\rho}\tilde{u}_i\tilde{u}_j + \bar{p}\delta_{ij} - \tilde{\tau}_{ij} - \tilde{\tau}_{ij}^{\text{sgs}} \\ (\bar{\rho}\tilde{E} + \bar{p})\tilde{u}_j + \tilde{q}_j + \tilde{q}_j^{\text{sgs}} - \tilde{u}_i(\tilde{\tau}_{ij} + \tilde{\tau}_{ij}^{\text{sgs}}) \end{bmatrix}, \tag{2}$$

where the subgrid-scale terms $\tilde{q}_j^{\text{sgs}}$ and $\tilde{\tau}_{ij}^{\text{sgs}}$ are closed by the Wall Adapted Local Eddy-viscosity (WALE) model [41].

The computational domain $\Omega$ is divided into boundary conforming elements. Inside each element, the governing equations are transformed into the reference domain as

$$\frac{\partial \hat{\mathbf{q}}}{\partial t} + |\mathbf{J}|^{-1}\hat{\nabla} \cdot \hat{\mathbf{F}} = 0, \tag{3}$$

where $\mathbf{J}$ is the transformation Jacobian, $\hat{\mathbf{q}}(\hat{x},t) = \mathbf{q}(x,t)$ and $\hat{\mathbf{F}} = |\mathbf{J}|\mathbf{J}^{-1} \cdot \mathbf{F}$ are the transformed solution and flux, respectively. The solution and flux functions are approximated by piece-wise discontinuous polynomials defined through interpolation of data at predefined solution points in each element. On the interfaces, the common numerical flux is approximated using an approximate Riemann solver with solutions from both sides of the interface. Then, a correction function is added so that the divergence of flux on the solution points are corrected using numerical flux on the interface to recover a global solution. The semi-discretized form of the scheme takes the form

$$\frac{\mathrm{d}\hat{\mathbf{q}}}{\mathrm{d}t} = -|\mathbf{J}|^{-1} \left[ \hat{\nabla} \cdot \hat{\mathbf{F}}^{\delta} + \sum_{i=1}^{N_i} \sum_{j=1}^{N_f} \hat{\nabla} \cdot g_{i,j}(\hat{\mathbf{x}}) \left( \hat{\mathbf{F}}_{i,j}^{\delta I \perp} - \hat{\mathbf{F}}_{i,j}^{\delta \perp} \right) \right], \tag{4}$$

where $N_i$ and $N_f$ are the number of interfaces on each element and number of flux points on each interface, respectively. The correction function, the transformed numerical flux, and the normal transformed discontinuous flux on the interface are represented by $g$, $\hat{\mathbf{F}}^{\delta I \perp}$, and $\hat{\mathbf{F}}^{\delta \perp}$, respectively. The solution is advanced in time using the strong stability-preserving Runge Kutta methods [42].

In a supersonic jet simulation, shocks often appear and cause numerical instability. Therefore, a shock capturing method based on Persson's method [43] was implemented together with a modal exponential filter [44] to stabilize the solution.

### *2.2. Wall Model*

In HiFiLES, a compressible wall stress model for the adiabatic non-slip wall is implemented to approximate the correct wall shear stress. Following Huang and Coakley [45], the law of the wall can be written in the same form as the incompressible case with an equivalent velocity $u_c$ defined by the Van Driest transformation [46]. Assuming a logarithmic wall function [47], the compressible wall function is

$$u_c^+ = \frac{u_c}{u_\tau} = \frac{1}{\kappa} \ln(y^+) + C \tag{5}$$

where $C = 5.2$, $\kappa = 0.42$, $u_\tau = \sqrt{\tau_w/\rho_w}$, and $y^+ = \rho_w u_\tau y/\mu_w$. Here, $\rho_w$ is the density on the wall, $\mu_w$ is the dynamic viscosity on the wall, and $\tau_w$ is the wall

shear stress. Assuming the wall is adiabatic, the Van Driest transformation velocity $u_c$ is

$$u_c = \sqrt{2C_pT_w}\sin^{-1}\left(\frac{|\mathbf{u}_\parallel - \mathbf{u}_w|}{\sqrt{2C_pT_w}}\right), \tag{6}$$

where $\mathbf{u}_\parallel$ is the wall parallel velocity at the input point. In order to avoid a log-layer mismatch, the flow solution of the wall-farthest point of the wall adjacent element is used in Eq. (6) [48]. The magnitude of wall shear stress can then be solved iteratively using Newton's method.

### *2.3. Proper Orthogonal Decomposition*

We use POD to extract the large-scale coherent structures associated with the noise source of BBSAN. The full spatial-temporal formulation from the original work of Lumley [49] is used. Following the computational method of Towne et al. [50], the discrete eigenvalue problem for solving POD at a frequency $f_k$ is given as

$$\mathbf{S}_{f_k}\mathbf{W}\mathbf{\Phi}_{f_k} = \mathbf{\Phi}_{f_k}\mathbf{\Lambda}_{f_k}, \tag{7}$$

where $\mathbf{\Lambda}_{f_k}$ is a diagonal matrix with eigenvalues corresponding to the extracted modes ranked in descending order, $\mathbf{\Phi}_{f_k}$ is a unitary matrix where the columns are POD modes, $S_{f_k}$ is the cross-spectral density of flow-field data, and $W$ is a diagonal matrix to account for both quadrature and energy weights.

To save computational time, the modes are calculated directly by performing a singular value decomposition [51] as

$$\sqrt{\mathbf{W}/N_b}\hat{\mathbf{Q}}_{f_k} = \left(\sqrt{\mathbf{W}}\mathbf{\Phi}_{f_k}\right)\mathbf{\Sigma}_{f_k}\mathbf{\Psi}^{\mathrm{H}}_{f_k}, \tag{8}$$

where $N_b$ is the number of flow realizations, $\hat{\mathbf{Q}}$ is the Fourier transformed flow-field data, columns of $\mathbf{\Phi}_{f_k}$ contain the first $N_b$ eigenvectors of $\mathbf{S}_{f_k}$, $\mathbf{\Sigma}_{f_k}$ is a diagonal matrix containing the corresponding eigenvalues, and the superscript H represents Hermitian transpose. After the modes are obtained, the flow-field can be recovered using a truncated expansion

$$q^{(l)}(\mathbf{x}, k\Delta t) = \sum_{m=1}^{N_f}\sum_{n=1}^{N_m} a^{(l)}_{mn}\Phi_{mn}\mathrm{e}^{2\pi\mathrm{i}(m-1)(k-1)/N_f}, \tag{9}$$

where $a_{mn}$ is the coefficient associated with the $n^{\text{th}}$ mode and the $m^{\text{th}}$ frequency component and $N_m$ is the number of modes used for the reconstruction. The coefficients $a$ are calculated with

$$a_{f_k}^{(l)} = \hat{\mathbf{Q}}_{f_k}^{(l)} \mathbf{W} \mathbf{\Phi}_{f_k}^{\mathrm{H}}. \tag{10}$$

The modes extracted using POD are ranked by variance (or energy) and the coherency of the modes is not guaranteed by definition. In turbulent flows, coherent velocities are not necessarily the most energetic ones [4]. Therefore, in the present work, the BBSAN source term in Eq. (15) is used in the POD analysis to extract coherent structures.

We characterize the BBSAN source as the inner product of the source term

$$I_{\mathrm{BBSAN}} \sim \int |\hat{\Theta}_s(\mathbf{x}, f)|^2 \mathrm{d}\mathbf{x}, \tag{11}$$

where $\hat{\Theta}_s(\mathbf{x}, f)$ is a source term introduced in the next section. High amplitude BBSAN requires the noise source being energetic. The mechanism of BBSAN proposed by Tam and Tanna [15] suggests that the sources should also be coherent so that the constructive interference effect is observed in the far-field. Accordingly, the optimal POD modes of the source term should be the coherent structures associated with BBSAN. Compared to the statistical model by Patel and Miller [33], the use of time resolved data from LES solutions removes the empiricism introduced by the modeling of turbulence within the RANS closure.

### *2.4. Time-Domain Acoustics Model for BBSAN*

Miller [32] developed a solution for acoustic fluctuations from a turbulent field governed by the Navier-Stokes equations. The field variables $\mathbf{q}$, including density, velocity, and pressure are decomposed into four components as $\mathbf{q} = \overline{\mathbf{q}} + \hat{\mathbf{q}} + \check{\mathbf{q}} + \mathbf{q}'$, where the overline symbol represents the time-averaged base flow, the check symbol indicates the isotropic component, the hat symbol indicates the anisotropic component, and a prime symbol denotes the radiating acoustic component of the variable. The decomposed variables are substituted into the Navier-Stokes equations. The equations are rearranged such that the radiating quantities are kept on the left-hand side, while the base flow and aerodynamic fluctuating quantities are brought to the right-hand side. The left-hand side terms are known as propagators and the right-hand side terms are the equivalent source terms. The source terms on the

right-hand side are

$$\Theta_0 = -\frac{\partial \underline{\rho}}{\partial t} - \frac{\partial \underline{\rho}\underline{u}_j}{\partial x_j}, \tag{12}$$

$$\Theta_i = -\frac{\partial \underline{\rho}\underline{u}_i}{\partial t} - \frac{\partial \underline{\rho}\underline{u}_i\underline{u}_j}{\partial x_j} - \frac{\partial \underline{p}}{\partial x_j}\delta_{ij} + \frac{\partial}{\partial x_j}\left[\mu\left(\frac{\partial \underline{u}_i}{\partial x_j} + \frac{\partial \underline{u}_j}{\partial x_i}\right)\right] - \frac{2}{3}\frac{\partial}{\partial x_j}\left[\mu\frac{\partial \underline{u}_k}{\partial x_k}\right], \tag{13}$$

and

$$\begin{aligned}\Theta_4 = &-\frac{\partial \underline{p}}{\partial t} - \frac{\gamma-1}{2}\frac{\partial \underline{\rho}\underline{u}_k\underline{u}_k}{\partial t} - \gamma\frac{\partial \underline{u}_j\underline{p}}{\partial x_j} - \frac{\gamma-1}{2}\frac{\partial \underline{\rho}\underline{u}_j\underline{u}_k\underline{u}_k}{\partial x_j} \\ &+ (\gamma-1)\frac{\partial}{\partial x_j}\left[\frac{c_p\mu}{Pr}\frac{\partial \underline{T}}{\partial x_j}\right] + (\gamma-1)\frac{\partial}{\partial x_j}\left[\mu\underline{u}_i\left(\frac{\partial \underline{u}_i}{\partial x_j} + \frac{\partial \underline{u}_j}{\partial x_i}\right)\right] \\ &- \frac{2}{3}(\gamma-1)\delta_{ij}\frac{\partial}{\partial x_j}\left[\mu\underline{u}_i\frac{\partial \underline{u}_k}{\partial x_k}\right],\end{aligned} \tag{14}$$

where $\Theta_0$ represents the source terms from the continuity equation, $\Theta_i$ (where $i = 1, 2, 3$) represents the three components of the source terms from momentum equations, and $\Theta_4$ represents the source terms from the energy equation. The under-bar symbol from Eq. (12) to (14) denotes the sum of the base quantity and the fluctuating quantities, i.e. $\underline{q} = \overline{q} + \hat{q} + \check{q}$.

All noise sources are presented on the right-hand side as source terms. Based on the physics and scaling analysis of the shock-associated noise, Patel and Miller [33] identified the source term responsible for BBSAN, which is

$$\Theta_s = -\gamma\hat{u}_j\frac{\partial \overline{p}}{\partial y_j}. \tag{15}$$

Here, the source term for BBSAN is the scalar product of the mean pressure gradient and anisotropic velocity, where the gradient of mean pressure denotes the shock-strength and the anisotropic velocity represents the large-scale turbulent structures. The model was validated in the frequency domain with measured data. The source term for fine-scale noise is also obtained using the same approach [52], which is identical to that used by Tam and Auriault [53] except for a coefficient which is derived analytically. To evaluate the source term of BBSAN, the velocity fluctuations associated with large-scale structures are extracted from the total fluctuations. In the work

of Patel and Miller [33], the anisotropic large-scale velocity fluctuations were modeled using theoretical and experimental results of Ishihara et al. [54].

A time-domain approach is used in the present work where the acoustic pressure fluctuation at the observer location is obtained by convolving the vector Green's function with the source terms as

$$p'(\mathbf{x},t) = \iint \sum_{n=0}^{4} g_{p,n}(\mathbf{x}-\mathbf{y},t-\tau)\Theta_n(\mathbf{y},\tau)\mathrm{d}\tau\mathrm{d}\mathbf{y}, \tag{16}$$

where $g_{p,n}$ is the vector Green's function of acoustic pressure associated with source term $\Theta_n$, $\mathbf{x}$ is the observer location, and $\mathbf{y}$ is the source location. The subscript $n$, where $n = 0$ to 4 denotes the component of vector Green's function and the source terms from the continuity, momentum, and energy equations.

In the present work, the pressure fluctuation associated with BBSAN is directly calculated using Eq. (16), where the source term is replaced by the identified BBSAN source term given in Eq. (15). For simplicity, we neglect the effect of refraction. The Green's function of acoustic pressure associated with the BBSAN source term is

$$\hat{g}_{p,s}(\mathbf{x}-\mathbf{y},t-\tau) = -\frac{1}{4\pi c_\infty^2|\mathbf{x}-\mathbf{y}|}\frac{\partial}{\partial t}(\delta(t-\tau)). \tag{17}$$

Substituting the BBSAN source term from Eq. (15) and corresponding Green's function from Eq. (17) into Eq. (16), we obtain

$$p'(\mathbf{x},t) = \iint \frac{1}{4\pi c_\infty^2|\mathbf{x}-\mathbf{y}|}\frac{\partial}{\partial t}(\delta(t-\tau))\gamma\hat{u}_j\frac{\partial\overline{p}}{\partial y_j}\mathrm{d}\tau\mathrm{d}\mathbf{y}. \tag{18}$$

The spectral density is obtained by multiplying the Fourier transform of time-domain acoustic pressure fluctuation with its complex conjugate.

## 3. Results

### *3.1. Computation Setup*

#### *3.1.1. Flow Configurations*

Two jet cases are considered in the current work. The first one is an unheated over-expanded supersonic jet that matches the experiment conducted in the anechoic jet facility at the Mechanical and Aerospace Engineering Department at University of Florida. The nozzle used in this case is bi-conic

and similar to one designed under the Department of Defense Strategic Environmental Research and Development Program (SERDP). This simulation and results are referred to as the "SERDP case." The second case is a heated under-expanded supersonic jet simulated and validated in the previous paper [40]. The nozzle geometry is NASA's baseline small metal chevron converging nozzle (SMC000) and will be referred to as the SMC000 case.

Both nozzles have a $D = 0.0508$ m exit diameter. The SERDP nozzle has design Mach number $M_d = 1.764$ and lip thickness $h_{\text{lip}} = 0.01D$. The SMC000 nozzle has design Mach number $M_d = 1.0$ and lip thickness $h_{\text{lip}} = 0.025D$. Table 1 presents the operation conditions of the jet cases, where $\text{Re}_D$ is the Reynolds number based on the nozzle diameter, the subscript $o$ represents total conditions, and the subscript $\infty$ represents ambient conditions.

| Name | $p_o/p_\infty$ | $T_o/T_\infty$ | $T_j$ [K] | $M_j$ | $u_j$ [m/s] | $\text{Re}_D$ |
|---|---|---|---|---|---|---|
| SERDP | 2.78 | 1.00 | 216.65 | 1.30 | 383.82 | $2.23 \times 10^6$ |
| SMC000 | 3.51 | 3.20 | 670.40 | 1.47 | 762.39 | $6.26 \times 10^5$ |

Table 1: Jet configurations.

*3.1.2. Computational Domain and Mesh*

The computational domain of both simulations are the same, which is a conical frustum located from $x/D = -6$ to $x/D = 60$, with radius of $r/D = 30$ and $r/D = 37.25$, respectively. The origin of the domain is located at the center of the nozzle exit plane and the nozzle geometry is included in the domain. The mesh refinement parameters of two simulations are presented in Table. 2. For more details of the SMC000 mesh, please refer to Shen and Miller [40].

For the SERDP case, an unstructured mesh with approximately 3.2 millions tetrahedral elements is used. A schematic of the computational mesh is shown in Fig. 1, where elements are highlighted by edge length in inches and the refinement regions are outlined. Similar to the SMC000 mesh, the SERDP mesh is isotropically refined in the jet exhaust region and the acoustic near-field region, which is defined by two conical frustums.

The jet exhaust refinement region starts from the nozzle exit at $x/D = 0$ and extends to $x/D = 17.5$. It has an initial radius $r/D = 0.5$ at the nozzle outlet and the divergence rate is 0.11, which follows the spreading rate of the jet exhaust to enclose the turbulent flow. The acoustic near-field refinement

region is from $x/D = 0$ to $x/D = 35$, with initial radius at nozzle exit $r/D = 1.5$. The spreading rate of this region is 0.129, which is slightly larger than the jet spreading rate. The FWH surface is placed between those two regions to predict far-field noise. Near the nozzle outlet, the mesh is refined with an additional constraint of $\Delta x/D \leq 0.0125D$ to capture the strong Mach disk expected at the over-expanded operating condition. Outside of these refined regions, the mesh is coarsened quickly to reduce the computational cost.

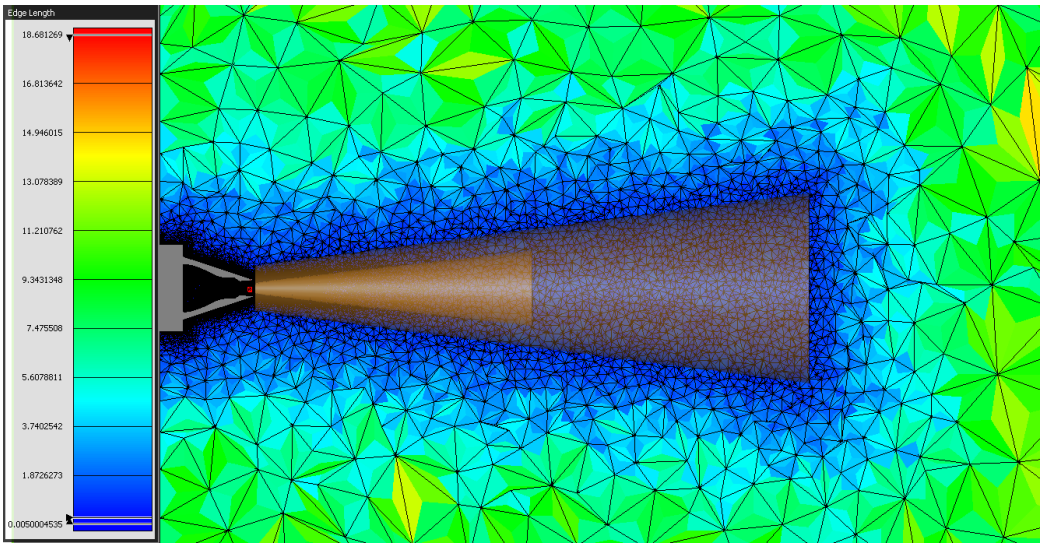


Figure 1: Schematic of computational mesh.

| Name | $\Delta x/D$ Flow region | | $\Delta x/D$ Near-field region | | $\Delta y/D$ on nozzle wall | Total number of elements |
|---|---|---|---|---|---|---|
| | Begin | End | Begin | End | | |
| SERDP | 0.025 | 0.3 | 0.3 | 0.3 | 0.0025 | $3.2 \times 10^6$ |
| SMC000 | 0.025 | 0.35 | 0.075 | 0.45 | 0.01 | $2.5 \times 10^6$ |

Table 2: Mesh refinement parameters.

### *3.1.3. Boundary Conditions*

For both simulations, the internal and exterior walls of the nozzle are adiabatic non-slip walls. For the SERDP case, flow separation will be triggered by the first shock inside of the nozzle because of the over-expanded

operating condition. Therefore, an anisotropic wall layer with initial layer thickness equivalent to $y^+ = 225$ is used, so that the turbulent boundary layer and flow separation can be captured accurately with the compressible wall model described in Section. 2.2. A Riemann invariant far-field boundary condition is used for all external boundaries of the computational domain in both simulations. This boundary condition is effective in suppressing the spurious reflections introduced by the acoustic waves exiting the domain. Compared to the recently developed non-reflecting boundary conditions [55], the present boundary condition has difficulty dealing with large-scale turbulent fluctuations due to the local linearization [56]. The newly developed method is insensitive to reflections because it integrates the field-variables in the volume of the jet plume. This is unlike FWH methods that rely on surface integrals through the acoustic field. Also, the external boundary of the computational domain is far away from the nozzle exit, where the turbulent jet exhaust becomes weak and the spurious reflections will not contaminate the solution. Therefore, it is reasonable to use the Riemann invariant far-field boundary condition for the external boundary.

*3.1.4. FWH Surface*

In the SERDP case, the FWH surface is defined following the guidance by Mendez et al. [57] and Lyrintzis [58]. This methodology has been validated with the SMC000 case by Shen and Miller [40]. The FWH surface for the SERDP case is the same as the one used in the SMC000 case. A pressure based formulation of the FWH equation proposed by Sparlart and Shur [59] is solved to obtain the pressure time history at the observer location in the far-field and to reduce the error caused by heating and the omission of the quadruple source term.

*3.1.5. Simulation Strategy*

The LES code uses the Message Passing Interface (MPI) to parallelize the simulation on a massive distributed memory system. The simulations are run on the supercomputer HiPerGator 2 at University of Florida with 2480 cores. The total run time is approximately 1600 hours. The correction function used in the SERDP case recovers a fourth-order spectral difference scheme, so that acoustic waves can be resolved up to $St = 1.48$ in the near-field region. Here, we are assuming that eight points per wavelength are necessary to resolve an acoustic wave (as suggested by Brès and Nichols [60]).

### *3.2. Validation of Over-expanded Jet Simulation*

The validation of the SMC000 case has been performed by Shen and Miller [40]. Hence, we only present the validation of the SERDP case in this section. First, the qualitative comparison of the flow-field visualizations is performed with the experimental schlieren. Then, the far-field acoustic predictions from the simulation are validated with experimental measurements.

#### *3.2.1. Flow-field Visualization*

Instantaneous plots of the vorticity magnitude are shown in Fig. 2 for the SERDP case. The vorticity magnitude is used to highlight the turbulence in the jet plume. Fig. 2(a) shows the vorticity magnitude on the $z/D = 0$ plane. The computational mesh is presented side by side in Fig. 2(b) to illustrate that the turbulent jet plume is completely enclosed in the mesh refinement region. Fig. 2(c) presents the vorticity magnitude on the cross-flow plane at the nozzle outlet. It is evident that the boundary layer at the nozzle outlet is turbulent and flow separation is also observed after the first shock-wave inside the nozzle.

Figure 3 shows the acoustic field on the $z/D = 0$ plane for the SERDP case. The acoustic field is visualized using instantaneous pressure. High wavenumber pressure waves with high amplitude are observed mainly near the nozzle exit, which are also observed by Liu et al. [61]. In the present simulation, the jet acoustic field is dominated by Mach wave radiation, characterized by downstream propagating parallel pressure waves. The Mach wave radiation is generated by turbulent structures with a supersonic phase speed with respect to the ambient flow [62]. The intensity of the Mach waves in the SERDP case are weaker relative to the SMC000 case due to a smaller $u_j$ shown in Table. 1.

Inside of the potential core region (approximately $0 \leq x/D \leq 5$), an additional spherical wave pattern that radiates in all directions is observed. These waves are related to shock-cell structures as suggested by Brès et al. [24] and Papamoschou [63].

Figure 4 shows the schlieren images of the jet. The experimental schlieren is averaged over 1000 images sampled at 8810 Hz. The numerical schlieren is instantaneous due to the high computational cost of averaging. Two images are aligned to compare the shock positions. At the nozzle outlet, a Mach disk is formed due to the strong pressure mismatch and the complex shock system inside the bi-conic nozzle. The Mach disk in the LES is located slightly upstream when compared to the experimental results. This is mainly due

to the lack of grid resolution and the additional numerical dissipation introduced at the Mach disk by the shock capturing method for stabilization. In the downstream direction of the first Mach disk, periodic shock cells are accurately captured by the simulation relative to experimental shock positions. These shocks are much weaker than the initial Mach disk.

*3.2.2. Acoustics*

Figure 5 shows the comparison of far-field noise between the FWH predictions and experimental measurements. Strouhal number from $St = 0.01$ to $St = 4.0$ are presented. Experimental data are acquired on an arc with radius of $30D$ from $\phi = 30^\circ$ to $\phi = 130^\circ$, where $\phi$ is the angle measured from the jet downstream direction. Pressure signals are sampled at 102 kHz, and a total of 60 seconds of signal is obtained. The noise spectra are calculated using Welch's method [64]. The data are first segmented into partially overlapping windows, each having $100,000$ samples with $50,000$ samples overlapping between two adjacent windows. Before the noise spectra are calculated, a Hanning window is applied to each window to reduce aliasing. The agreement between the FWH predictions and experiments in the downstream directions (Figs. 5(a) to 5(c)) imply that the large-scale turbulent structures are accurately captured by the current LES.

In Figs. 5(d) to 5(f), corresponding to the sideline directions, the acoustic field is dominated by the fine-scale mixing noise. Slight over-prediction with the FWH equation of noise is observed from $St = 1$ to $St = 2$. The over-prediction is below a maximum of 3 dB.

Noise spectra at upstream directions, shown in Figs. 5(g) to 5(i), are dominated by BBSAN at mid to high frequencies. As the observer goes upstream, the BBSAN peak moves to lower frequency and increases in amplitude. The prediction from LES results capture the peak amplitude with maximum error within 3 dB. The small shift in peak frequencies relative to experiment are due to the discrepancy of shock positions predicted by the simulation due to numerical errors.

The overall sound pressure level (OASPL) of the SERDP case is shown in Fig. 6. The FWH predictions fit well with the experiment, especially at downstream and upstream angles, where the deviation is below 1 dB. The directivity pattern of the OASPL is also captured, where the downstream noise radiation is stronger than upstream. In the sideline direction, the FWH prediction over-predicts the experiment by up to 2.2 dB, which is within experimental uncertainty.

*3.3. Time-Domain BBSAN Predictions using the Full Field*

We substitute the full fluctuating quantities from the LES solutions into the time-domain Eq. (18) to obtain the preliminary prediction of BBSAN spectra. Figure 7 shows the predicted BBSAN spectra at 90° for both simulations labeled as "BBSAN with complete flow-field." These predictions are compared with the total spectra from the FWH prediction and experimental measurements. The BBSAN and fine-scale noise calculated from the statistical models are also presented for reference. The statistical models use RANS simulation results as an argument to compute the noise spectra in the far-field. More details of the statistical model for BBSAN and fine-scale noise can be found in Patel and Miller [33, 52].

The BBSAN peak frequencies of the primary lobe in both cases are accurately predicted using the time-domain method. However, in Fig. 7(a), the BBSAN spectrum only captures part of the lobe and the peak amplitude is 5 dB lower than that in the total spectrum. This problem is not observed in Fig. 7(b), where both the lobe width and peak amplitude are captured accurately. This is probably because the oblique shocks in the SMC000 case are strong and stable, while the shock waves in the SERDP case are weak and highly oscillatory. Therefore, a large portion of shock noise in the SERDP case is produced by the fluctuating pressure rather than the time-averaged pressure used in the current study. At lower frequencies, the BBSAN magnitude of the SERDP case using the current method is approximately 10 dB lower than the total noise, while in the SMC000 case, the low frequency components have similar noise levels as the total spectrum. A major advantage of the time-domain approach is that BBSAN spectra of both cases do not decay like those of the statistical model using the RANS solutions. This is because the LES captures many large-scale unsteady motions, which is completely absent in the steady RANS predictions. The SMC000 case contains screech, which is predicted in Fig. 7(b). Screech is captured by the current method because the generation mechanism of screech is similar to that of the BBSAN, according to Tam [65]. The discrete screech peaks are formed by the amplification of flow instabilities through a feedback loop and the steady RANS solutions do not capture this phenomenon. In addition, the current results use the full unsteady velocity field in the source term, so that the BBSAN spectra may include contributions from other noise components.

The present method does not use any empirical coefficients as used in the steady RANS based approaches by Miller [32], Patel and Miller [33], or others. The errors introduced by modeling the large-scale coherent structures in the

previous methods are eliminated by directly using the time domain flow-field solution from the LES simulation and a time-domain BBSAN model.

### *3.4. POD Results*

A coarser structured grid is sampled in the computational domain for POD to save computational time. The POD configurations and sampling parameters are shown in Table 3, where $\Delta h$ is the distance between the grid points. The distance between grid points in the sampling domain is constant in all directions. The size of the Fourier window, the number of overlapping snapshots between neighboring windows, and the number of realizations are represented by $n_f$, $n_o$, and $n_b$, respectively. The sampling domain is a structured cubic grid, centered about the jet axis and starting from the nozzle outlet at $x/D = 0$. The sampled domain encompasses the whole jet potential core. According to Podboy et al. [66], the majority of BBSAN sources are enclosed in this region.

| Name | $\Delta t$ [s] | $n_x$ | $n_y$ | $n_z$ | $\Delta h/D$ | $n_f$ | $n_o$ | $n_b$ |
|---|---|---|---|---|---|---|---|---|
| SERDP | $1.0 \times 10^{-5}$ | 300 | 100 | 100 | 0.05 | 256 | 128 | 16 |
| SMC000 | $5.5 \times 10^{-6}$ | 130 | 61 | 61 | 0.1 | 720 | 360 | 16 |

Table 3: Sampling parameters and POD configurations.

Eigenvalue spectra from the POD results for both simulations are shown in Fig. 8. Since the eigenvalue spectra are symmetric about $f = 0$, only positive frequencies are presented. The eigenvalues of each mode number are plotted as a function of frequency, although the coherent structures extracted by the same mode number at different frequencies have no obvious connections [67]. For each frequency component, the eigenvalues are sorted in descending order of modal energy so that the first mode at a frequency extracts the most energy. POD results are presented this way to show how the energy is distributed across different frequencies in the jet flow. At high frequencies the energy extracted by the optimal mode is usually lower than that of lower frequencies.

In Fig. 8(a), the optimal modes from $St = 0.2$ to $St = 1.1$ extracts significantly more energy than the subsequent modes. In other words, the eigenvalue spectra show low rank behavior at these frequencies. This frequency range overlaps the region corresponding to BBSAN. This implies that in the SERDP simulation, the BBSAN spectra can be recovered with the source

field reconstructed with the first few modes. The spectra in Fig. 8(b) are similar to Fig. 8(a), except at $St = 0.2$, $St = 0.4$, and $St = 0.8$, where the optimal POD mode captures the dominant amount of energy at these frequencies. These frequencies correspond to the harmonics of the fundamental screech frequency observed in the previous work [40].

Contour plots of the POD modes show the spatial distribution of energy per mode. The energy distribution can reveal the noise generation mechanism by these modes. Figure 9 shows the first and the second POD modes for the SERDP simulation at $St = 1.0$, corresponding to the peak BBSAN frequency observed at 90°. The peak BBSAN frequency is estimated from the FWH prediction at the same observation angle. The coherent structures extracted by the optimal mode shown in Fig. 9(a) exhibit high energy throughout the potential core region from $x/D = 0.5$ to $x/D = 4$. The quasi periodicity of the energy distribution in the $x$-direction will form a strong directivity in the noise spectrum due to the constructive interference effect of noise emitted at different source locations. This mode extracts the coherent structures related to BBSAN. The second mode (Fig. 9(b)) and subsequent modes (not shown here), do not exhibit spatial coherency and thus will not form highly directive noise radiation. Therefore, these modes should not contribute to BBSAN.

Figure 10 shows the first and second POD modes at $St = 0.4$ in the SMC000 simulation. This frequency is both the second harmonic of the fundamental screech frequency and the BBSAN peak frequency at 90°. The first mode shown in Fig. 10(a) exhibits high energy at the first few oblique shocks. However, for the second mode shown in Fig. 10(b), the energy is mainly located near the end of potential core from $x/D = 5$ to $x/D = 8$. Both the first and second mode show strong spatial coherency.

In order to separate the POD modes corresponding to the large-scale coherent structures associated with BBSAN from other incoherent sources, the directivity of the BBSAN generated by each POD mode is studied. The BBSAN is calculated by substituting the source term reconstructed with the individual POD mode into Eq. (18), and the power spectral density is then averaged azimuthally over 24 evenly distributed stations. Figure 11 shows the BBSAN intensity calculated by each POD mode at the peak BBSAN frequency observed from 90° as a function of observer angle. The results from 20° to 150° are plotted.

In Fig. 11(a), corresponding to the SERDP case, the first mode shows a very steep rise of noise intensity around 95°, which becomes the dominant mode at the sideline directions. This directivity pattern also agrees with the

directivity of the dominant BBSAN source at this frequency. The subsequent modes, nevertheless, show much weaker directivity. Therefore, we conclude that the first mode is the large-scale coherent structure that generates the BBSAN at this frequency.

In Fig. 11(b) corresponding to the SMC000 case, the first mode dominates over a wide range of directions including the low downstream angles from 20° to 40° and sideline to upstream angles from 60° to 120°. This agrees with the characteristic of the second harmonic of screech tone observed in the total spectra [40]. The second mode, highlighted by the red line, shows high BBSAN intensity around 100° and generates more than 3 times stronger acoustic power than the rest of the modes. We conclude that the second mode corresponds to the large-scale structure that generates BBSAN. In addition, a low angle radiation around 35° by this mode with similar intensity is also observed. This can be interpreted that in some situations a portion of BBSAN also radiates in the downstream direction. However, we have only observed this phenomenon in the present computational study. To the authors' knowledge, it has not yet been reported in the literature. We hope that further evidence can be gathered in future computations or experiments.

In order to validate our assumption that the source of BBSAN can be represented solely by the leading POD modes, the BBSAN spectra calculated from different number of modes at 90° are presented in Fig. 12. The results show good agreement between our reduced order approximation and the total spectra predicted by the FWH equation. For both simulations, the BBSAN peak is recovered when only the leading POD mode is used to calculate the spectrum. This result confirms our assumption that only the large-scale coherent structures are responsible for the generation of BBSAN.

*3.4.1. Source Distribution*

In this section, we calculate the source intensity contours of BBSAN. The source intensity is calculated using the frequency domain form of Eq. (16), which is

$$I_s(y,f) = \hat{g}_{p,s}(\mathbf{x},\mathbf{y};f)\hat{\Theta}_s(\mathbf{y},f)\int \hat{g}^*_{p,s}(\mathbf{x},\mathbf{z};f)\hat{\Theta}^*_s(\mathbf{z},f)\mathrm{d}\mathbf{z}. \tag{19}$$

The magnitude of source intensity is calculated and averaged over all the flow realizations. It is azimuthally averaged over 24 evenly spaced stations. Figures 13 and 14 show the magnitude of source intensity observed from 90°

at the peak BBSAN frequency for both cases. The noise intensity is calculated with the reconstructed BBSAN source using one mode, two modes, and all modes, respectively. The distribution of sources in both figures are similar to the POD modes shown in Fig. 8, where the majority of the source intensity is observed inside the potential core. In Fig. 13, the source distribution is captured using only one POD mode. Increasing the number of modes only increase the source intensity uniformly throughout the domain. In Fig. 14, the source intensity calculated from the leading POD mode is mainly concentrated on the first few oblique shocks. When the source term is reconstructed using the first two POD modes, the source intensity near the end of the potential core is increased. This agrees with the observation by Podboy et al. [66], who measured the source location of BBSAN of a similar heated under-expanded jet at the same observation angle using a beamforming technique. Hence, the present method is capable of predicting the important source locations of BBSAN.

## 4. Conclusion

In the present paper, an unheated over-expanded supersonic jet from the SERDP program is simulated and validated using experimental schlieren and acoustic measurements. The BBSAN is analyzed using data from LES and a previous LES of a heated under-expanded supersonic jet from NASA. The BBSAN source term consists of large-scale coherent anisotropic velocity fluctuations multiplied by the gradient of mean pressure. In the present work, the anisotropic source components are obtained directly by decomposing the LES source field using POD and reconstructing it using a different number of modes. A directivity study of the POD modes shows that the large-scale coherent structures associated with the BBSAN are extracted with the first few POD modes. The BBSAN spectra are predicted using a new time-domain approach with the reconstructed source field. The shape of the primary BBSAN lobes observed from 90° are recovered using only the leading POD modes for both jet cases. In addition, the present method captures some large-scale flow phenomena, which are absent in the RANS solutions such as screech tones. The BBSAN source distribution at the peak BBSAN frequency observed from $\phi = 90°$ is captured by the source field reconstructed with only the first two POD modes for both jet cases. The source distribution agrees with the experimental work by Podboy et al. [66] and by Breen and Ahuja [68].

**Acknowledgements**

This research was supported by the Office of Naval Research Grant No. N00014-17-1-2583. Any opinions, findings, and conclusions or recommendations expressed in this material are those of the author(s) and do not necessarily reflect the views of the Office of Naval Research. The authors are grateful for experimental data from Professor Ukeiley's Unsteady Fluid Dynamics Group at the University of Florida.

[1] J. Doychak, Department of Navy Jet Noise Reduction Project Overview, in: 15th Annual Partners in Environmental Technology Technical Symposium and Workshop, Washington D.C., 2010.
URL `https://apps.dtic.mil/dtic/tr/fulltext/u2/a553981.pdf`

[2] J. E. Ffowcs Williams, Hydrodynamic noise, Annual Review of Fluid Mechanics 1 (1) (1969) 197–222.

[3] A. A. Townsend, The Structure of Turbulent Shear Flow, Cambridge University Press, 1980.

[4] A. F. Hussain, Role of coherent structures in turbulent shear flows, Proceedings of the Indian Academy of Sciences Section C: Engineering Sciences 4 (2) (1981) 129. doi:10.1007/BF02896739.

[5] G. L. Brown, A. Roshko, On density effects and large structure in turbulent mixing layers, Journal of Fluid Mechanics 64 (4) (1974) 775–816. doi:10.1017/s002211207400190x.

[6] P. E. Dimotakis, G. L. Brown, The mixing layer at high reynolds number: large-structure dynamics and entrainment, Journal of Fluid Mechanics 78 (3) (1976) 535–560. doi:10.1017/s0022112076002590.

[7] E. Mollo-Christensen, Jet noise and shear flow instability seen from an experimenter's viewpoint, Journal of Applied Mechanics 34 (1) (1967) 1–7. doi:10.1115/1.3607624.

[8] C. K. W. Tam, Supersonic jet noise, Annual Review of Fluid Mechanics 27 (1) (1995) 17–43. doi:10.1146/annurev.fl.27.010195.000313.

[9] C. K. W. Tam, K. C. Chen, A statistical model of turbulence in two-dimensional mixing layers, Journal of Fluid Mechanics 92 (2) (1979) 303–326. doi:10.1017/s002211207900063x.

[10] C. K. W. Tam, P. J. Morris, The radiation of sound by the instability waves of a compressible plane turbulent shear layer, Journal of Fluid Mechanics 98 (2) (1980) 349–381. doi:10.1017/s0022112080000195.

[11] C. K. W. Tam, D. E. Burton, Sound generated by instability waves of supersonic flows. part 1. two-dimensional mixing layers, Journal of Fluid Mechanics 138 (1984) 249. doi:10.1017/s0022112084000112.

[12] C. K. W. Tam, D. E. Burton, Sound generated by instability waves of supersonic flows. part 2. axisymmetric jets, Journal of Fluid Mechanics 138 (1984) 273. doi:10.1017/s0022112084000124.

[13] P. Jordan, T. Colonius, Wave packets and turbulent jet noise, Annual Review of Fluid Mechanics 45 (1) (2013) 173–195. doi:10.1146/annurev-fluid-011212-140756.

[14] M. Harper-Bourne, M. J. Fisher, The noise from shock waves in supersonic jets, AGARD conference proceedings No. 131, 1973, pp. 1–11.

[15] C. K. W. Tam, H. K. Tanna, Shock associated noise of supersonic jets from convergent-divergent nozzles, Journal of Sound and Vibration 81 (3) (1982) 337–358. doi:10.1016/0022-460x(82)90244-9.

[16] C. K. W. Tam, Stochastic model theory of broadband shock associated noise from supersonic jets, Journal of Sound and Vibration 116 (2) (1987) 265–302. doi:10.1016/s0022-460x(87)81303-2.

[17] P. J. Morris, S. A. E. Miller, Prediction of broadband shock-associated noise using reynolds-averaged navier-stokes computational fluid dynamics, AIAA Journal 48 (12) (2010) 2931–2944. doi:10.2514/1.j050560.

[18] T. Suzuki, Wave-packet representation of shock-cell noise for a single round jet, AIAA Journal 54 (12) (2016) 3903–3917. doi:10.2514/1.j055097.

[19] D. C. Wilcox, Turbulence Modeling for CFD, Vol. 2, DCW industries La Canada, CA, 1998.

[20] H. Choi, P. Moin, Grid-point requirements for large eddy simulation: Chapman's estimates revisited, Physics of Fluids 24 (1) (2012) 011702. doi:10.1063/1.3676783.

[21] J. E. F. Williams, D. L. Hawkings, Sound generation by turbulence and surfaces in arbitrary motion, Philosophical Transactions of the Royal Society A: Mathematical, Physical and Engineering Sciences 264 (1151) (1969) 321–342. doi:10.1098/rsta.1969.0031.

[22] B. Boersma, S. Lele, Large eddy simulation of a mach 0.9 turbulent jet, in: 5th AIAA/CEAS Aeroacoustics Conference and Exhibit, American Institute of Aeronautics and Astronautics (AIAA), AIAA Paper No. 99-1874, 1999. doi:10.2514/6.1999-1874.

[23] M. Shur, P. Spalart, M. Strelets, A. Garbaruk, Further steps in LES-based noise prediction for complex jets, in: 44th AIAA Aerospace Sciences Meeting and Exhibit, American Institute of Aeronautics and Astronautics (AIAA), AIAA Paper No. 2006-485, 2006. doi:10.2514/6.2006-485.

[24] G. A. Brès, F. E. Ham, J. W. Nichols, S. K. Lele, Unstructured large-eddy simulations of supersonic jets, AIAA Journal 55 (4) (2017) 1164–1184. doi:10.2514/1.j055084.

[25] S. Mendez, M. Shoeybi, A. Sharma, F. E. Ham, S. K. Lele, P. Moin, Large-eddy simulations of perfectly expanded supersonic jets using an unstructured solver, AIAA Journal 50 (5) (2012) 1103–1118. doi:10.2514/1.j051211.

[26] J. Liu, A. T. Corrigan, K. Kailasanath, N. S. Heeb, D. E. Munday, E. J. Gutmark, Computational study of shock-associated noise characteristics using LES, in: 19th AIAA/CEAS Aeroacoustics Conference, American Institute of Aeronautics and Astronautics (AIAA), AIAA Paper No. 2013-2199, 2013. doi:10.2514/6.2013-2199.

[27] G. A. Brès, V. Jaunet, M. L. Rallic, P. Jordan, T. Colonius, S. K. Lele, Large eddy simulation for jet noise: The importance of getting the boundary layer right, in: 21st AIAA/CEAS Aeroacoustics Conference, American Institute of Aeronautics and Astronautics (AIAA), AIAA Paper No. 2015-2535, 2015. doi:10.2514/6.2015-2535.

[28] J. Liu, A. T. Corrigan, Large-eddy simulations of supersonic jet noise generation using wall modeling, in: 2018 AIAA/CEAS Aeroacoustics Conference, American Institute of Aeronautics and Astronautics (AIAA), AIAA Paper No. 2018-3943, 2018. doi:10.2514/6.2018-3943.

[29] J. Liu, R. Ramamurti, Numerical study of supersonic jet noise emanating from an f404 nozzle at model scale, in: AIAA Scitech 2019 Forum, American Institute of Aeronautics and Astronautics (AIAA), AIAA Paper No. 2019-0807, 2019. doi:10.2514/6.2019-0807.

[30] A. T. Corrigan, A. Kercher, J. Liu, K. Kailasanath, Jet noise simulation using a higher-order discontinuous galerkin method, in: 2018 AIAA Aerospace Sciences Meeting, American Institute of Aeronautics and Astronautics (AIAA), AIAA Paper No. 2018-1247, 2018. doi:10.2514/6.2018-1247.

[31] S. C. Spiegel, J. R. DeBonis, H. Huynh, Overview of the NASA Glenn flux reconstruction based high-order unstructured grid code, in: 54th AIAA Aerospace Sciences Meeting, American Institute of Aeronautics and Astronautics (AIAA), AIAA Paper No. 2016-1061, 2016. doi:10.2514/6.2016-1061.

[32] S. A. E. Miller, Noise from isotropic turbulence, AIAA Journal 55 (3) (2017) 755–773. doi:10.2514/1.j055114.

[33] T. K. Patel, S. A. E. Miller, Statistical sources for broadband shock-associated noise using the Navier-Stokes equations, The Journal of the Acoustical Society of America 146 (6) (2019) 4339–4351. doi:10.1121/1.5139216.

[34] M. R. López, A. Sheshadri, J. R. Bull, T. D. Economon, J. Romero, J. E. Watkins, D. M. Williams, F. Palacios, A. Jameson, D. E. Manosalvas, Verification and validation of HiFiLES: a high-order LES unstructured solver on multi-GPU platforms, in: 32nd AIAA Applied Aerodynamics Conference, AIAA Paper No. 2014-3168, 2014. doi:10.2514/6.2014-3168.

[35] H. T. Huynh, A flux reconstruction approach to high-order schemes including discontinuous galerkin methods, in: 18th AIAA Computational Fluid Dynamics Conference, American Institute of Aeronautics and Astronautics (AIAA), AIAA Paper No. 2007-4079, 2007. doi:10.2514/6.2007-4079.
URL `https://doi.org/10.2514/6.2007-4079`

[36] P. E. Vincent, P. Castonguay, A. Jameson, A new class of high-order energy stable flux reconstruction schemes, Journal of Scientific Comput-

ing 47 (1) (2010) 50–72. doi:10.1007/s10915-010-9420-z.
URL https://doi.org/10.1007/s10915-010-9420-z

[37] P. Castonguay, P. E. Vincent, A. Jameson, A new class of high-order energy stable flux reconstruction schemes for triangular elements, Journal of Scientific Computing 51 (1) (2011) 224–256. doi:10.1007/s10915-011-9505-3.
URL https://doi.org/10.1007/s10915-011-9505-3

[38] P. Castonguay, D. Williams, P. Vincent, A. Jameson, Energy stable flux reconstruction schemes for advection–diffusion problems, Computer Methods in Applied Mechanics and Engineering 267 (2013) 400 – 417. doi:https://doi.org/10.1016/j.cma.2013.08.012.

[39] H. T. Huynh, A reconstruction approach to high-order schemes including discontinuous galerkin for diffusion, in: 47th AIAA Aerospace Sciences Meeting including The New Horizons Forum and Aerospace Exposition, American Institute of Aeronautics and Astronautics (AIAA), AIAA Paper No. 2009-403, 2009. doi:10.2514/6.2009-403.

[40] Shen, Weiqi and Miller, Steven A. E., Validation of a High-order Large Eddy Simulation Solver for Acoustic Prediction of Supersonic Jet Flow, Journal of Theoretical and Computational AcousticsAccepted - To Appear (2019). doi:10.1142/S2591728519500233.

[41] F. Nicoud, F. Ducros, Subgrid-scale stress modelling based on the square of the velocity gradient tensor, Flow, turbulence and Combustion 62 (3) (1999) 183–200. doi:10.1023/a:1009995426001.

[42] D. I. Ketcheson, Highly efficient strong stability-preserving runge–kutta methods with low-storage implementations, SIAM Journal on Scientific Computing 30 (4) (2008) 2113–2136. doi:10.1137/07070485x.
URL https://doi.org/10.1137/07070485x

[43] P.-O. Persson, Shock capturing for high-order discontinuous galerkin simulation of transient flow problems, in: 21st AIAA Computational Fluid Dynamics Conference, American Institute of Aeronautics and Astronautics (AIAA), AIAA Paper No. 2013-3061, 2013. doi:10.2514/6.2013-3061.

[44] J. S. Hesthaven, R. M. Kirby, Filtering in legendre spectral methods, Mathematics of Computation 77 (263) (2008) 1425–1452. doi:10.1090/s0025-5718-08-02110-8.

[45] P. Huang, T. Coakley, Calculations of supersonic and hypersonic flows using compressible wall functions, in: Engineering Turbulence Modelling and Experiments, Elsevier, 1993, pp. 731–739. doi:10.1016/b978-0-444-89802-9.50072-1.
URL https://doi.org/10.1016/b978-0-444-89802-9.50072-1

[46] E. R. V. Driest, Turbulent boundary layer in compressible fluids, Journal of the Aeronautical Sciences 18 (3) (1951) 145–160. doi:10.2514/8.1895.

[47] F. M. White, I. Corfield, Viscous fluid flow, Vol. 3, McGraw-Hill New York, 2006.

[48] A. Frère, C. C. de Wiart, K. Hillewaert, P. Chatelain, G. Winckelmans, Application of wall-models to discontinuous galerkin LES, Physics of Fluids 29 (8) (2017) 085111. doi:10.1063/1.4998977.
URL https://doi.org/10.1063/1.4998977

[49] J. L. Lumley, The structure of inhomogeneous turbulence, in: Atmospheric Turbulence and Wave Propagation, 1967, pp. 166–178.

[50] A. Towne, O. T. Schmidt, T. Colonius, Spectral proper orthogonal decomposition and its relationship to dynamic mode decomposition and resolvent analysis, Journal of Fluid Mechanics 847 (2018) 821–867. doi:10.1017/jfm.2018.283.

[51] K. Taira, S. L. Brunton, S. T. M. Dawson, C. W. Rowley, T. Colonius, B. J. McKeon, O. T. Schmidt, S. Gordeyev, V. Theofilis, L. S. Ukeiley, Modal analysis of fluid flows: An overview, AIAA Journal 55 (12) (2017) 4013–4041. doi:10.2514/1.j056060.

[52] Patel, Trushant K. and Miller, Steven A. E., Source of Fine-Scale Turbulent Mixing Noise using the Navier-Stokes Equations, AIAA Journal - Technical Notes(Under Review) (2020).

[53] C. K. W. Tam, L. Auriault, Jet Mixing Noise from Fine-Scale Turbulence, AIAA Journal 37 (2) (1999) 145–153. doi:10.2514/2.691.

[54] T. Ishihara, K. Yoshida, Y. Kaneda, Anisotropic Velocity Correlation Spectrum at Small Scales in a Homogeneous Turbulent Shear Flow, Phys. Rev. Lett. 88 (15) (2002) 154501. doi:10.1103/PhysRevLett.88.154501.

[55] A. Garai, L. Diosady, S. M. Murman, N. K. Madavan, Development of a perfectly matched layer technique for a discontinuous-galerkin spectral-element method, in: 54th AIAA Aerospace Sciences Meeting, American Institute of Aeronautics and Astronautics, 2016. doi:10.2514/6.2016-1338.

[56] M. B. Giles, Nonreflecting boundary conditions for euler equation calculations, AIAA Journal 28 (12) (1990) 2050–2058. doi:10.2514/3.10521.

[57] S. Mendez, M. Shoeybi, S. K. Lele, P. Moin, On the use of the ffowcs williams-hawkings equation to predict far-field jet noise from large-eddy simulations, International Journal of Aeroacoustics 12 (1-2) (2013) 1–20. doi:10.1260/1475-472x.12.1-2.1.

[58] A. S. Lyrintzis, M. Coderoni, The use of large eddy simulations in jet aeroacoustics, in: AIAA Scitech 2019 Forum, American Institute of Aeronautics and Astronautics (AIAA), AIAA Paper No. 2019-0633, 2019. doi:10.2514/6.2019-0633.
URL https://doi.org/10.2514/6.2019-0633

[59] P. R. Spalart, M. L. Shur, Variants of the ffowcs williams - hawkings equation and their coupling with simulations of hot jets, International Journal of Aeroacoustics 8 (5) (2009) 477–491. doi:10.1260/147547209788549280.

[60] G. Brès, J. Nichols, S. Lele, F. Ham, Towards best practices for jet noise predictions with unstructured large eddy simulations, in: 42nd AIAA Fluid Dynamics Conference and Exhibit, American Institute of Aeronautics and Astronautics (AIAA), AIAA Paper No. 2012-2965, 2012. doi:10.2514/6.2012-2965.

[61] J. Liu, K. Kailasanath, N. Heeb, D. Munday, E. Gutmark, Large-eddy simulations of a supersonic heated jet, in: 17th AIAA/CEAS Aeroacoustics Conference (32nd AIAA Aeroacoustics Conference), American

Institute of Aeronautics and Astronautics (AIAA), AIAA Paper No. 2011-2884, 2011. doi:10.2514/6.2011-2884.

[62] C. K. W. Tam, Mach wave radiation from high-speed jets, AIAA Journal 47 (10) (2009) 2440–2448. doi:10.2514/1.42644.

[63] D. Papamoschou, Mach wave elimination in supersonic jets, AIAA Journal 35 (10) (1997) 1604–1611. doi:10.2514/2.19.
URL https://doi.org/10.2514/2.19

[64] P. Welch, The use of fast fourier transform for the estimation of power spectra: A method based on time averaging over short, modified periodograms, IEEE Transactions on Audio and Electroacoustics 15 (2) (1967) 70–73. doi:10.1109/tau.1967.1161901.

[65] C. K. W. Tam, J. Seiner, J. Yu, Proposed relationship between broadband shock associated noise and screech tones, Journal of Sound and Vibration 110 (2) (1986) 309–321. doi:10.1016/s0022-460x(86)80212-7.

[66] G. G. Podboy, M. P. Wernet, M. M. Clem, A. F. Fagan, Noise source location and flow field measurements on supersonic jets and implications regarding broadband shock noise (2018). doi:10.13140/RG.2.2.23444.19847.

[67] O. T. Schmidt, A. Towne, G. Rigas, T. Colonius, G. A. Brès, Spectral analysis of jet turbulence, Journal of Fluid Mechanics 855 (2018) 953–982. doi:10.1017/jfm.2018.675.

[68] N. P. Breen, K. K. Ahuja, Supersonic Jet Noise Source Distributions, in: AIAA Scitech 2020 Forum, no. January, American Institute of Aeronautics and Astronautics, AIAA Paper No. 2020-0497, Reston, Virginia, 2020, pp. 1–23. doi:10.2514/6.2020-0497.

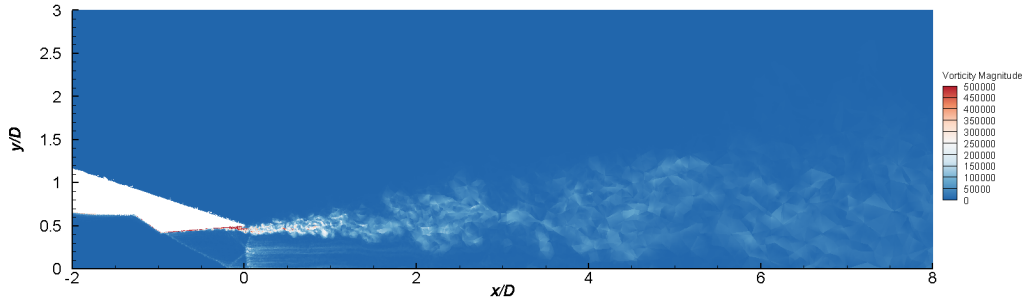


(a)

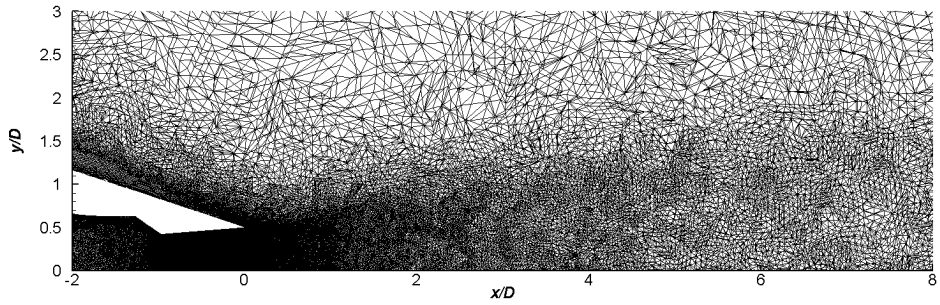


(b)

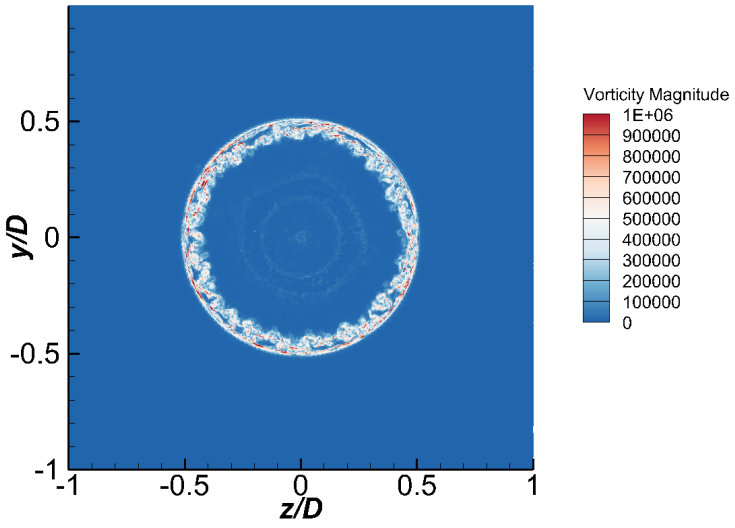


(c)

Figure 2: Instantaneous vorticity magnitude at (a) $z/D = 0$ plane with (b) computational mesh and on the (c) $x/D = 0$ crossflow plane for the SERDP case.

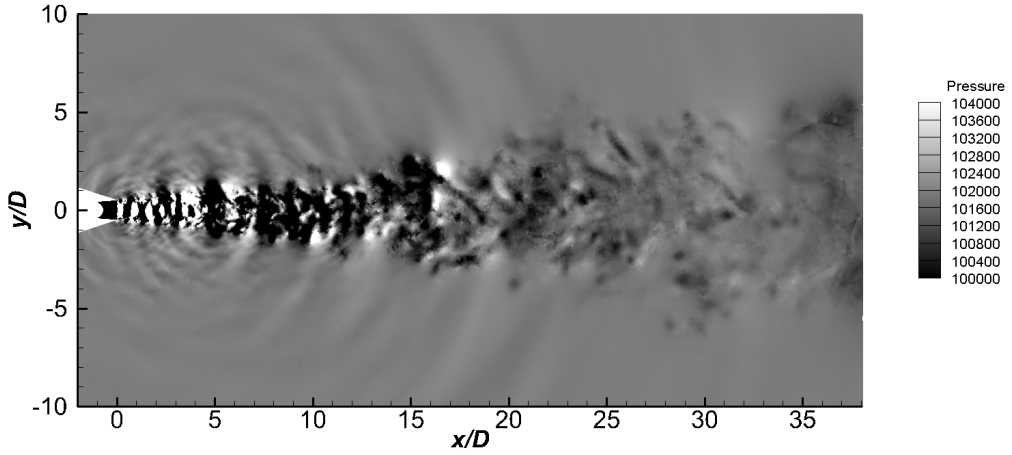


Figure 3: Acoustic pressure field at $z/D = 0$, unit Pascal.

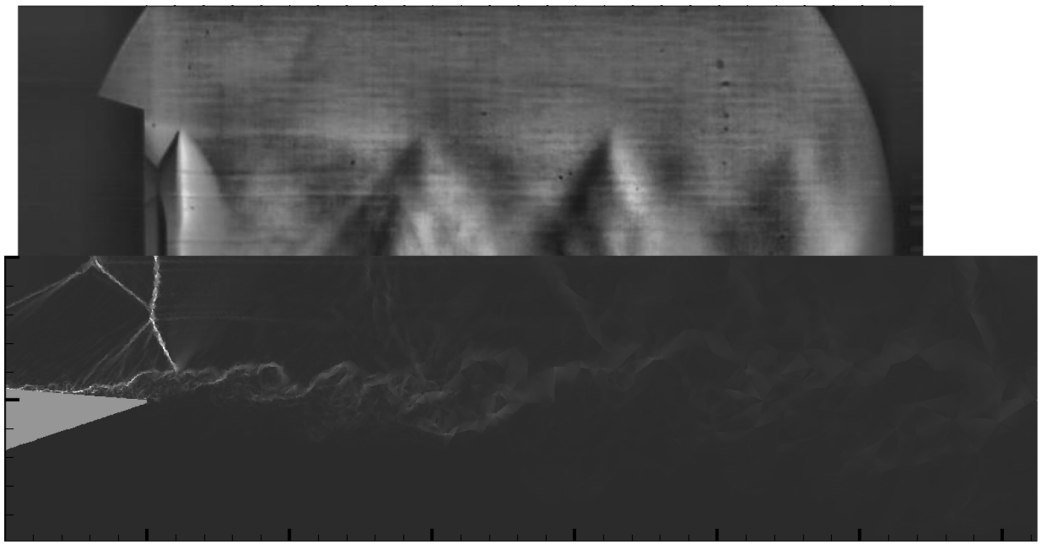

Figure 4: Comparison of schlieren between LES and experiment for the SERDP case.

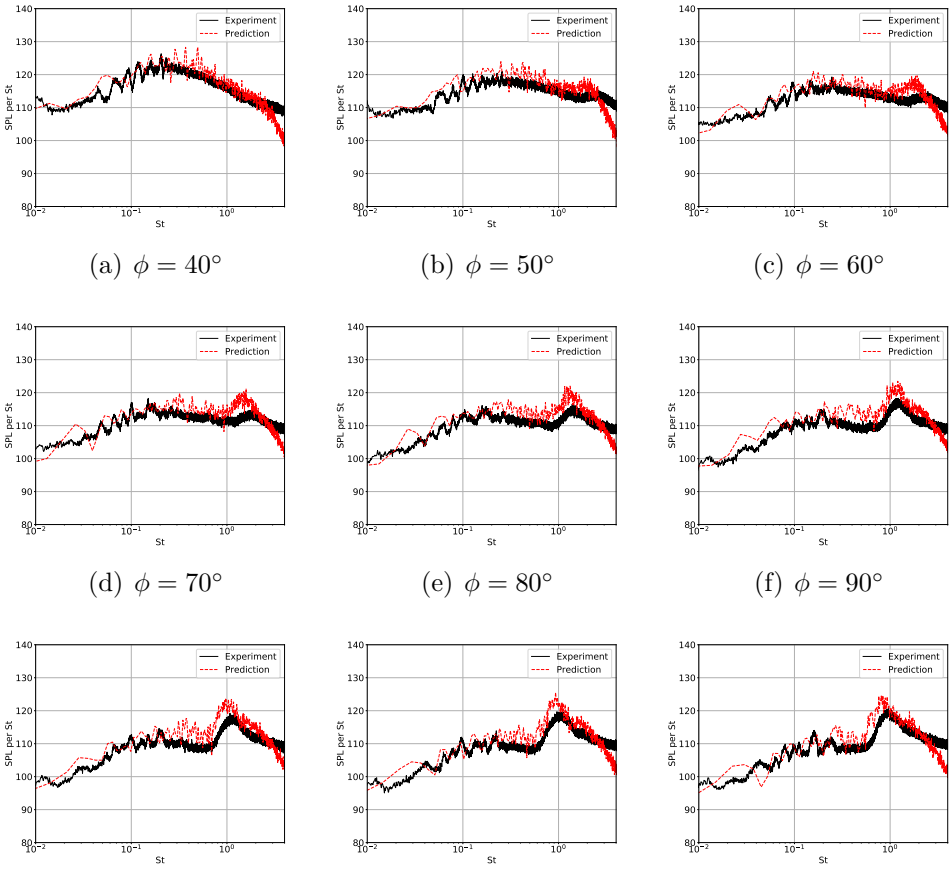


(a) $\phi = 40°$ (b) $\phi = 50°$ (c) $\phi = 60°$

(d) $\phi = 70°$ (e) $\phi = 80°$ (f) $\phi = 90°$

(g) $\phi = 100°$ (h) $\phi = 110°$ (i) $\phi = 120°$

Figure 5: Comparison of the far-field noise spectra obtained using the FWH method with the experimental measurements for the SERDP case.

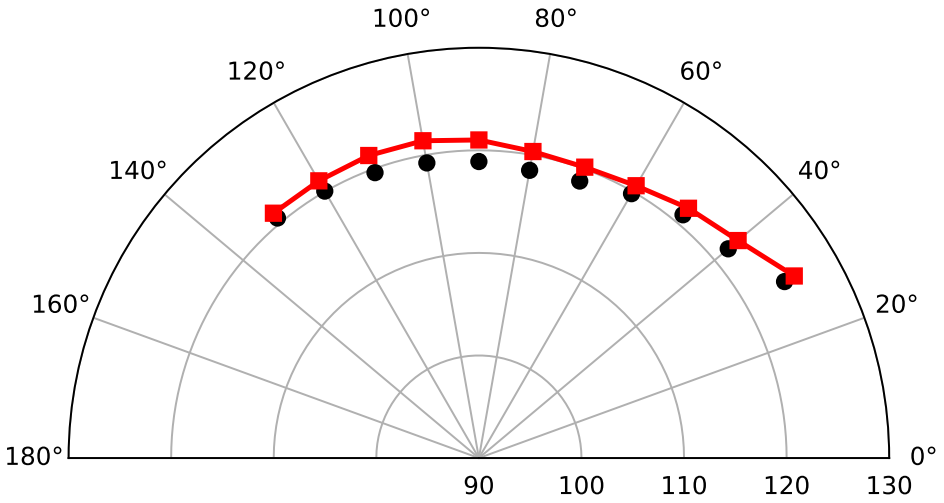


Figure 6: Comparison of the OASPL obtained from the FWH method using LES (line with square markers) with the experimental measurements (dots).

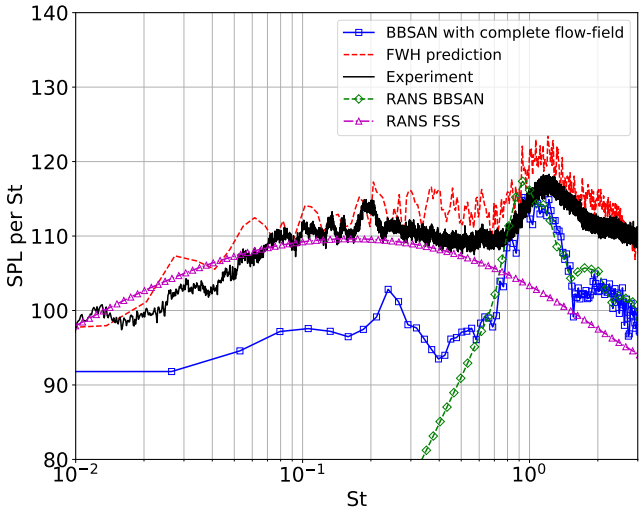


(a)

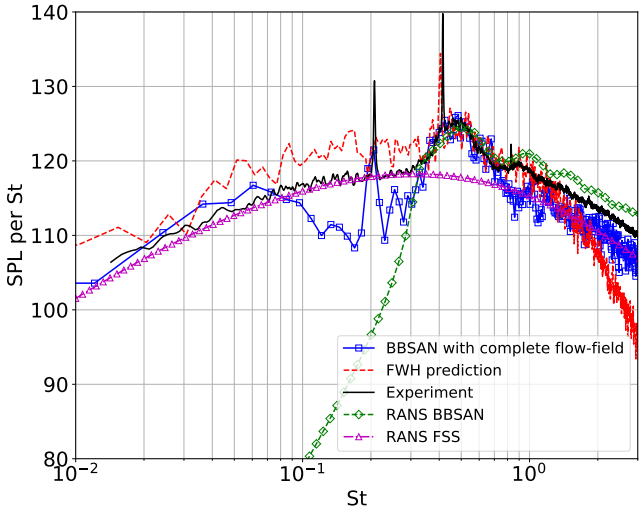


(b)

Figure 7: Time-domain based prediction of BBSAN at 90° for (a) SERDP case and (b) SMC000 case compared with total spectra from FWH prediction and experiment. RANS statistical prediction for BBSAN and fine-scale noise presented for reference.

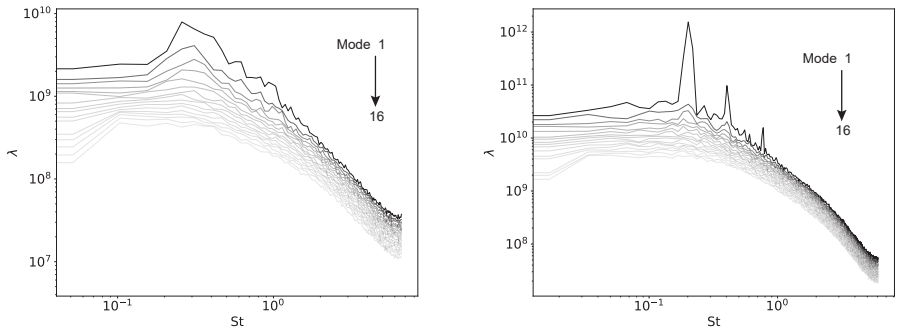


(a) (b)

Figure 8: POD eigenvalue spectra of the BBSAN source field in (a) SERDP case and (b) SMC000 case.

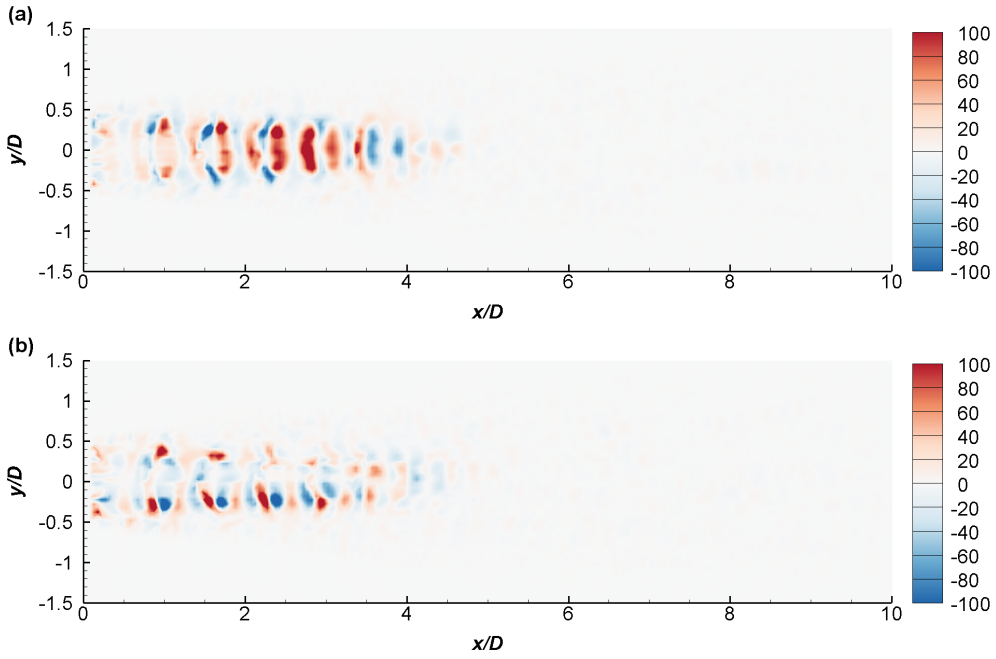


Figure 9: Contour plots of the real part of the (a) first and the (b) second POD mode of the SERDP case at peak BBSAN frequency at 90°, $St = 1.0$.

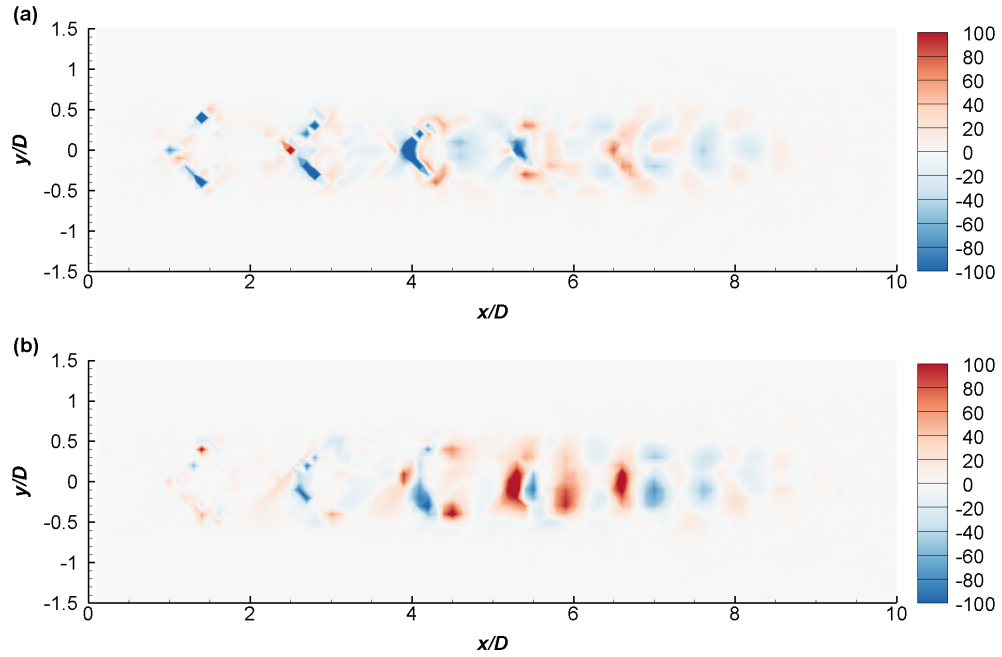


Figure 10: Contour plots of the real part of the (a) first and the (b) second POD mode of the SMC000 case at peak BBSAN frequency at 90°, $St = 0.4$.

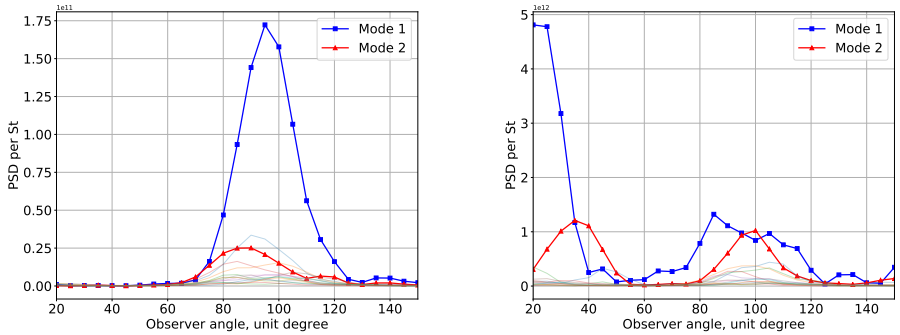


(a) (b)

Figure 11: BBSAN directivity of the POD modes at peak BBSAN frequency at 90° for (a) SERDP case and (b) SMC000 case. The first 2 modes are highlighted.

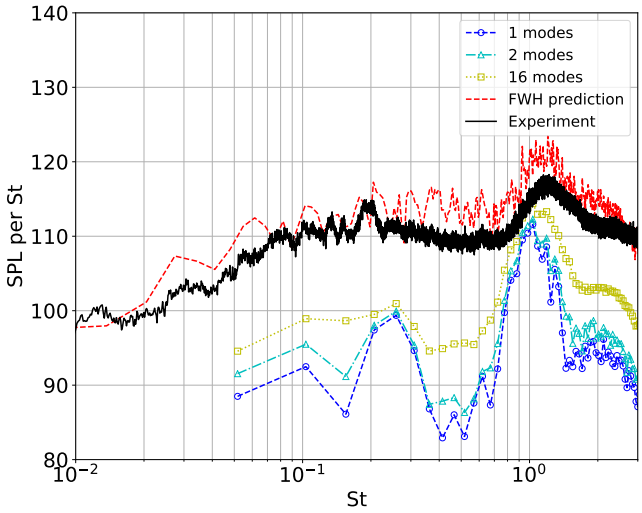


(a)

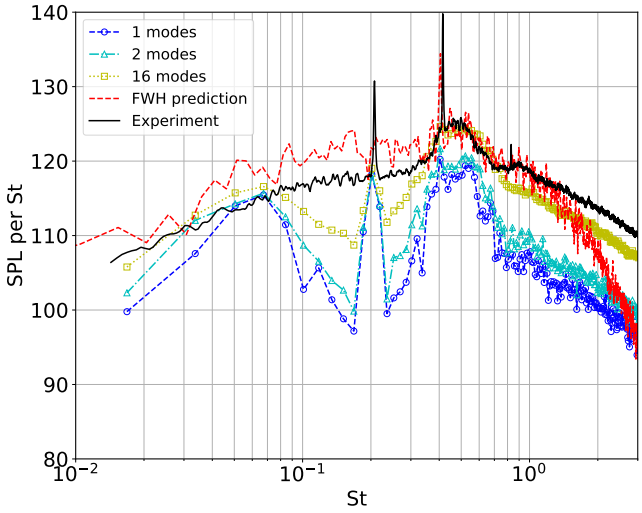


(b)

Figure 12: BBSAN spectra calculated from different number of modes at 90° for (a) SERDP case and (b) SMC000 case.

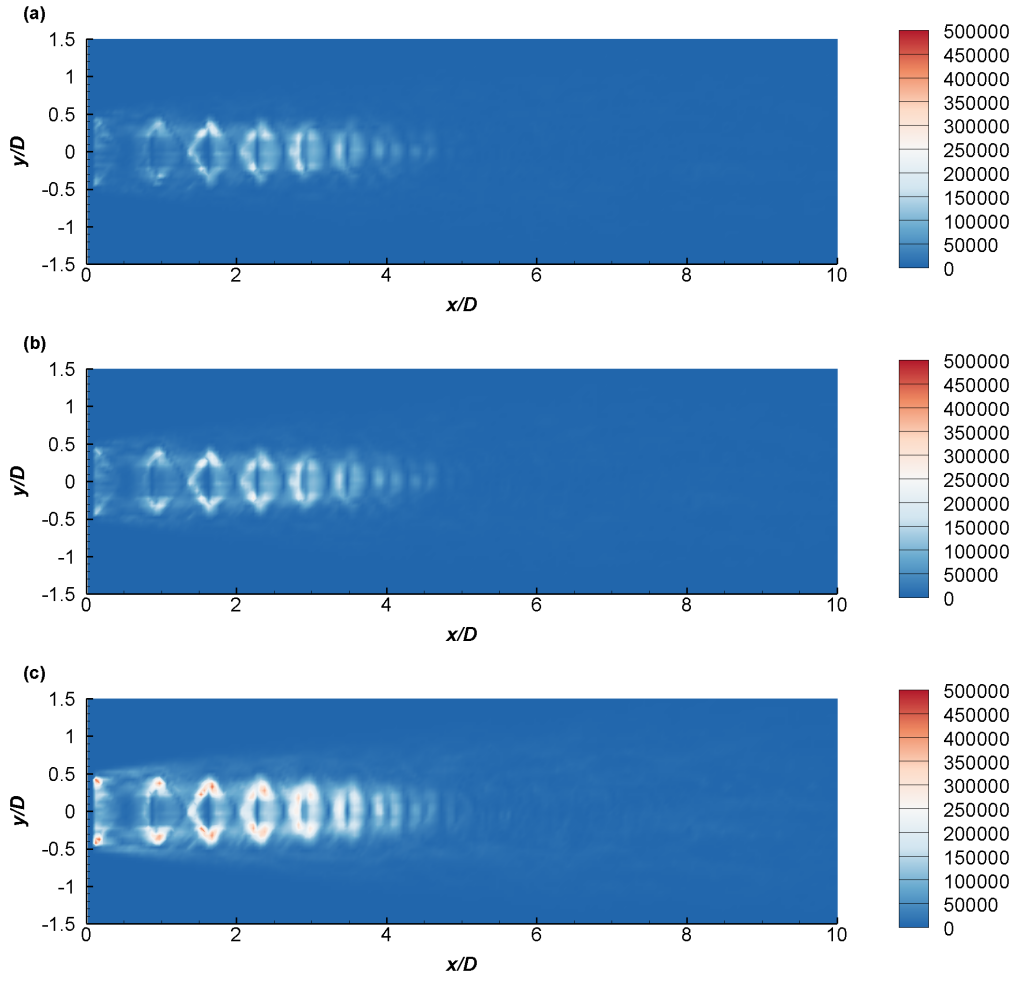


Figure 13: Contour of BBSAN source intensity observed from $\phi = 90°$ at peak BBSAN frequency for SERDP case ($St = 1.0$) using the BBSAN source reconstructed with (a) one mode, (b) two modes, and (c) all modes.

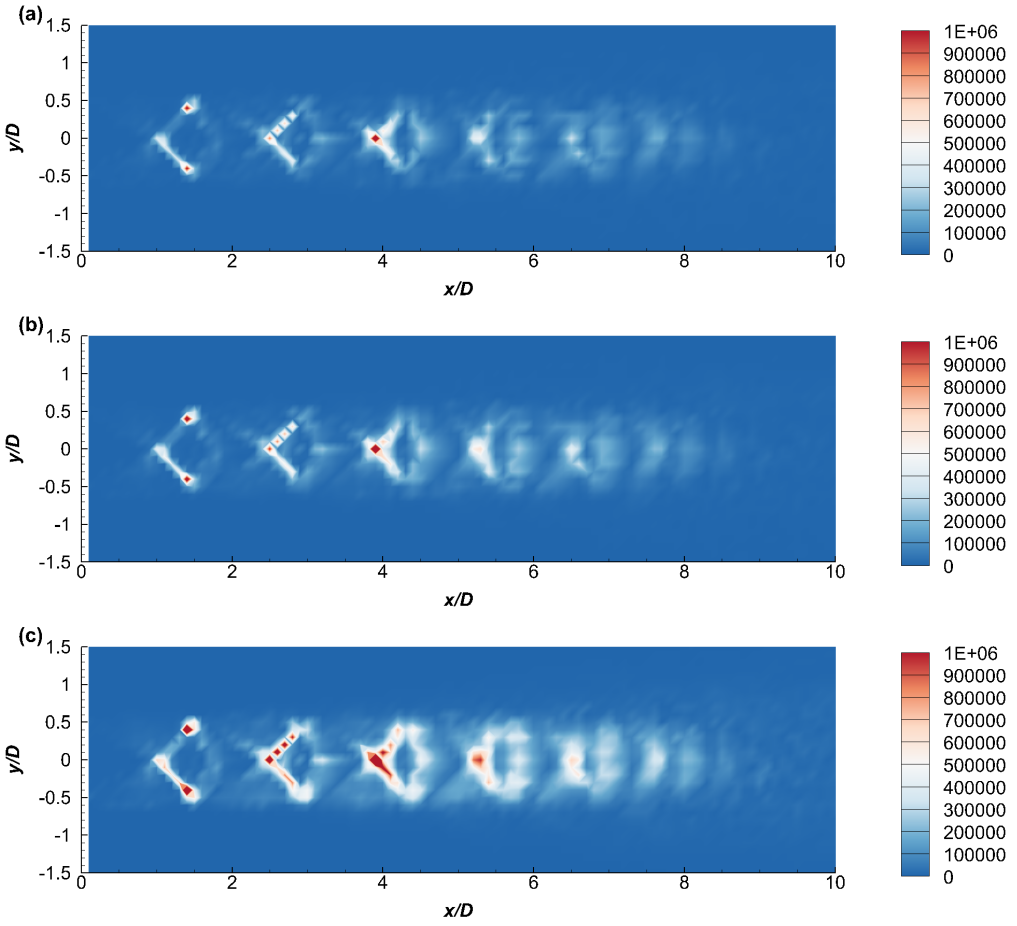


Figure 14: Contour of BBSAN source intensity observed from $\phi = 90°$ at peak BBSAN frequency for SMC000 case ($St = 0.4$) using the BBSAN source reconstructed with (a) one mode, (b) two modes, and (c) all modes.